PAPER

Check for updates

From cluster halides to catalysts: nanostructured molybdenum carbides for efficient hydrogen evolution reaction

Guillaume Dubois, [ID] [a] Sébastien Mathivet, [ID] [a] Noée Dumait,[a] Ludivine Rault,[b] Stéphane Cordier, [ID] *[a] Corinne Lagrost, [ID] *[ab] Fabien Grasset [ID] *[cd] and Franck Tessier [ID] *[a]

An original synthesis route for tailoring the hydrogen evolution reaction (HER) activity of α-Mo$_2$C-based catalysts is reported using soluble and air-stable halide precursors built from nanosized $[Mo_6Cl_{14}]^{2-}$ cluster units, namely $(H_3O)_2[Mo_6Cl_{14}]\cdot 7H_2O$ and $((n\text{-}C_4H_9)_4N)_2[Mo_6Cl_{14}]$, combined with sucrose as a biosourced carbon source. The resulting catalysts consist of nanosized α-Mo$_2$C crystallites embedded in residual carbon, with molybdenum preserved in the +2 oxidation state from the halide precursor to the final material. The chemical nature of the precursor strongly influences the phase composition, homogeneity, specific surface area, and morphology of the resulting α-Mo$_2$C powders. Among the synthesized materials, the catalyst derived from $((n\text{-}C_4H_9)_4N)_2[Mo_6Cl_{14}]$ exhibits the highest HER performance in alkaline media, characterized by the lowest overpotential at 10 mA cm^{-2}, the largest electrochemical surface area, and the smallest Tafel slope. Long-term electrochemical testing also reveals surface activation during operation, enhancing both activity and stability. These findings indicate that the catalytic behavior of α-Mo$_2$C cannot be attributed solely to nanostructuring effects but arises from a subtle interplay between crystallite size, porosity, and surface chemistry. The use of Mo$_6$ cluster-based precursors thus provides an effective and versatile approach to control the composition and molybdenum oxidation state of molybdenum carbides, enabling the design of advanced powder materials with optimized surface and electrocatalytic properties.

1. Introduction

Hydrogen (H$_2$) is considered as a promising energy carrier and a viable alternative to fossil fuels, particularly as a fuel source for hydrogen fuel cells for automotive or stationary applications. Hence, H$_2$ can serve as an efficient vehicle for storing energy in chemical form, addressing the need to store electricity generated from intermittent renewable sources such as wind, solar, and tidal power.

Water electrolysis offers a clean alternative for hydrogen generation, as it does not release greenhouse gases during the reaction itself. When produced by electrolysis using clean electricity from surplus renewable energy sources, hydrogen is referred to as "green" hydrogen.[1–3] The electrocatalytic hydrogen evolution reaction (HER) corresponds to the reduction of aqueous protons in acidic media or water in alkaline media by electrons in a catalytically-active cathode material to liberate H$_2$. Platinum group metals (Pt, Ir, Ru) and transition metals (Ni, Co) are commonly employed as catalysts, respectively.[4–6] Furthermore, Pt is widely recognized as a benchmark catalyst for evaluating electrocatalytic performance.[7,8] Given the current challenges of the energy transition, all these elements are listed as critical raw materials (CRM) by the European Union (EU).[9] Indeed, even if Ni does not meet the CRM thresholds of the EU, it was included in the CRM list of strategic raw materials in line with the CRM act. So, due to their high cost and/or their limited availability, the search for affordable and efficient alternatives remains essential.

In this context, the molybdenum carbides, MoC and Mo$_2$C, have emerged as promising low-cost catalysts for HER.[10–15] These materials exhibit high chemical and thermal stability, as well as surface reactivity, and show catalytic performance approaching that of noble metals. Besides a good chemical stability in a wide pH range, these materials and especially Mo$_2$C, as platinum, have good HER stability at low and high pH values (*i.e.* pH = 0 and pH = 14). The platinoid behavior of Mo carbide is related to the d orbitals of molybdenum that can

[a]*Univ. Rennes, CNRS, Institut des Sciences Chimiques de Rennes – UMR 6226, F-35000 Rennes, France. E-mail: Stephane.Cordier@univ-rennes.fr; Corinne.Lagrost@univ-rennes.fr; Franck.Tessier@univ-rennes.fr*

[b]*Univ. Rennes, CNRS, ScanMAT, UAR 2025, F-35000 Rennes, France*

[c]*CNRS-Saint-Gobain-NIMS, IRL 3629, Laboratory for Innovative Key Materials and Structures (LINK), National Institute for Materials Science (NIMS), Tsukuba, Ibaraki, 305-0044, Japan. E-mail: Fabien.Grasset@cnrs.fr*

[d]*NIMS-CNRS-Saint-Gobain International Collaboration Center, NIMS, Tsukuba, Ibaraki 305-0047, Japan*

expand upon hybridization with the s and p orbitals of carbon, resulting in a higher d-electron density states of Mo near to the Fermi level similarly to the d-band of Pt.[16,17] Molybdenum offers a cost-effective alternative to platinum and is not included on CRM list.

Despite their potential, designing of Mo_2C-based catalysts with electrocatalytic performance rivaling that of Pt remains a major challenge. Their main limitations are their low conductivity, poor crystallinity and low specific surface areas, which results in a low density of active sites. Considerable efforts have been undertaken to synthesize Mo_2C with optimized structural, morphological and surface features at the nanoscale.[13,18–20] Among the different allotropic forms of Mo_2C, the α-Mo_2C phase has been identified as the most efficient for the electrocatalytic HER activity.[12,21,22]

Enhancing the specific surface area through downsizing represents an effective strategy to improve the catalytic performance of carbides. Nevertheless, the carburization process typically requires high-temperature annealing, which frequently results in pronounced nanoparticle agglomeration, thereby diminishing the accessible surface area.[23] In addition, Mo carbide nanocrystals are often prone to aggregation owing to their intrinsically high surface energy.[24] The development of highly efficient HER electrocatalysts requires precise control over chemical composition, crystal structure, crystallite size, and morphology during synthesis. The results presented here demonstrate that, beyond conventional parameters such as carburization temperature or carbon source, the oxidation state and chemical nature of the Mo precursor play a decisive role in controlling the structure and morphology of α-Mo_2C—an effect that, to the best of our knowledge, has not yet been reported in the literature. To date, the most common Mo sources for preparing Mo_2C include Mo metal powder, molybdenum oxide (MoO_3), molybdenum chloride ($MoCl_5$), sodium molybdate (Na_2MoO_4) and ammonium heptamolybdate (($NH_4)_6Mo_7O_{24}\cdot4H_2O$).[18,25] It is worth noting that the oxidation state of molybdenum in the aforementioned precursors is typically either very low (Mo^0) or very high (Mo^{5+}/Mo^{6+}). Consequently, redox transformations are required to achieve the Mo^{2+} state, mandatory to obtain α-Mo_2C.

Herein, we describe a new route to design Mo carbides-based materials with high specific surface areas. Molybdenum cluster compounds – $(TBA)_2Mo_6Cl_{14}$ (TMC) and $(H_3O)_2Mo_6Cl_{14}\cdot7H_2O$ (HMC), where TBA stands for tetrabutylammonium (($C_4H_9)_4N^+$) – are investigated as innovative precursors for the synthesis of molybdenum carbides in the α-Mo_2C allotropic form. The use of these precursors based on nanometric cluster motifs containing Mo^{II} aims at promoting nanostructuring of Mo_2C materials,[26,27] thereby enhancing their electrocatalytic performance for the HER. This strategy is found to lead to powders (Mo_2C-HMC and Mo_2C-TMC) with high specific surface area and containing nanometric crystallites of α-Mo_2C phase, by employing relatively low carburization temperature (below 650 °C). The resulting powdered materials are thoroughly characterized by a combination of techniques (XRD, Raman, BET, XPS, TEM, SEM analyses). Their HER performances are evaluated and compared with that of α-Mo_2C prepared from ammonium

heptamolybdate built up from nanosized $[Mo^{VI}_7O_{24}]^{2-}$ as a reference (Mo_2C-AHM). This highlights the critical influence of structural parameters, molybdenum oxidation state and surface chemical composition on the catalytic performances.

2. Results and discussion

2.1. Syntheses and characterization of Mo_2C-AHM, Mo_2C-TMC and Mo_2C-HMC

The Mo_2C-AHM, Mo_2C-TMC and Mo_2C-HMC carbides based on the α-Mo_2C form were synthesized by adapting the protocol described by Vitale et al.[25] These authors have employed household sucrose as a carbon source and ammonium heptamolybdate tetrahydrate ($(NH_4)_6Mo_7O_{24}\cdot4H_2O$ (AHM) as molybdenum source, both dissolved in water, to prepare a coprecipitate that leads to cubic-phased Mo carbides at low carburization temperatures, i.e. 400 °C, under H_2 atmosphere. The protocol used by Vitale et al. allows the production of α-Mo_2C small crystallites but their specific surface area remains low ($\sim$1 m^2 g^{-1}).[25] The $(NH_4)_6Mo_7O_{24}\cdot4H_2O$ precursor is built up from the nanosized $[Mo^{VI}_7O_{24}]^{6-}$ heptamolybdate unit that exhibit an ellipsoid shape ($\sim$11.5 $\times$ 10 $\times$ 8 Å^3). In the crystal structure, they form layers oriented perpendicular to the y-axis ($P2_1/c$; a = 8.3934(8) Å; b = 36.1703(45) Å; c = 10.4715(11) Å; β = 115.958(8)°; V = 2858.3 Å^3; Z = 4) as represented in Fig. 1. Within these layers, cations and water molecules connect the
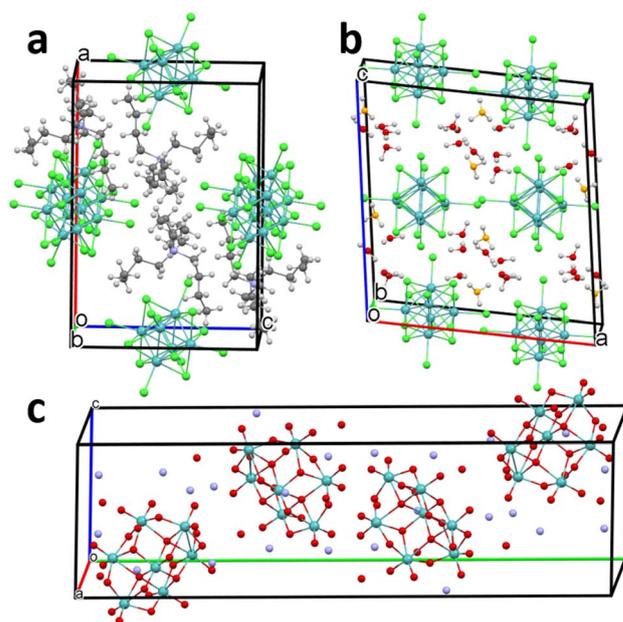

Fig. 1 Representation of the unit cells of (a) $(TBA)_2Mo_6Cl_{14}$ (TMC; $P2_1/n$; a = 12.764(3) Å; b = 11.663(2) Å; c = 18.490(4) Å; β = 90.14(2)°; Z = 2)), (b) $(H_3O)_2Mo_6Cl_{14}\cdot7H_2O$ (HMC; $C2/c$; a = 17.27(1) Å; b = 9.17(3) Å; c = 18.55(2) Å; β = 98(1)°; Z = 4) and (c) $((NH_4)_6Mo_7O_{24}\cdot4H_2O$, (AHM; $P2_1/c$; a = 8.3934(8) Å; b = 36.1703(45) Å; c = 10.4715(11) Å; β = 115.958(8)°; V = 2858.3 Å^3; Z = 4).[28–30] Molybdenum atoms are represented in blue, chlorine in green, oxygen from water molecules in red, oxygen from hydronium in orange, nitrogen in purple, carbon in dark grey and hydrogen in light grey. For the sake of clarity, hydrogen atoms are not represented for AHM.

This journal is © The Royal Society of Chemistry 2026

J. Mater. Chem. A, 2026, 14, 11332–11343 | 11333

heptamolybdate units through a complex network of ionic and hydrogen bonds.[22] This compound is highly soluble in water.

A distinctive feature of this study is the use of molybdenum cluster halides, $(TBA)_2Mo_6Cl_{14}$ and $(H_3O)_2Mo_6Cl_{14} \cdot 7H_2O$, as innovative molybdenum precursors for carbide synthesis. The crystal structures of $(H_3O)_2Mo_6Cl_{14} \cdot 7H_2O$[29–32] and $(TBA)_2Mo_6Cl_{14}$ are shown in Fig. 1a and b, respectively. The crystal structures of both compounds are built-up from anionic $[\{Mo_6Cl^i_8\}Cl^a_6]^{2-}$ cluster units composed of Mo^{II} atoms octahedra coordinated by 8 chlorine ligands in face-capping and 6 in terminal positions. The $[\{Mo_6Cl^i_8\}Cl^a_6]^{2-}$ cluster units exhibit a spherical shape with a diameter of about 11 Å. In $(TBA)_2Mo_6Cl_{14}$, the cohesion of the structure is due to interactions between hydrogen atoms from TBA^+ counter cations and halogen atoms from the cluster unit. In $(H_3O)_2Mo_6Cl_{14} \cdot 7H_2O$, oxonium groups are well localized and form a complex hydrogen bonding network with water crystallization molecules. The $[\{Mo_6Cl^i_8\}Cl^a_6]^{2-}$ units are trapped in this network and interacts with oxonium ions by terminal chlorine–hydrogen interactions. The nature of the counter cation has a drastic influence on the solubility $(H_3O)_2Mo_6Cl_{14} \cdot 7H_2O$ exhibits high solubility in ethanol and in acidic aqueous solutions, while $(TBA)_2Mo_6Cl_{14}$ is insoluble in water and ethanol but highly soluble in acetone, acetonitrile, THF, and various other organic solvents.

These cluster-based compounds are synthesized by a procedure combining solid state and solution chemistries as described previously.[28,33] α-Mo_2C based carbides were prepared by adjusting the synthesis parameters, the C/Mo ratio and carburization temperatures for the three selected precursors. The optimized syntheses are described in detail in the experimental section. Note that owing to the different counter cation composition of the cluster compounds, $(TBA)_2Mo_6Cl_{14}$ is dissolved in acetone and added to an aqueous solution of sucrose whereas $(H_3O)_2Mo_6Cl_{14} \cdot 7H_2O$ clusters were dissolved in a solution of ethanol before addition to a solution of sucrose in water. After evaporation of solvent and drying, the resulting solid-state products were ground and heated under Ar : H_2 (95%:5%) flow. For comparison purposes, Mo_2C-AHM was prepared from $(NH_4)_6Mo_7O_{24} \cdot 4H_2O$, using a protocol adapted from Vitale *et al.* and used as a reference.[25] It should be noted that the reduction of Mo(VI) to Mo(II) must occur for the formation of Mo_2C when using AHM, whereas in HMC and TMC molybdenum is already present in the +II oxidation state.

The X-ray diffraction (XRD) patterns of Mo_2C-TMC, Mo_2C-HMC and Mo_2C-AHM materials are shown in Fig. 2. All three diffraction patterns correspond to the α-Mo_2C phase (ICDD 01-071-0242) (Fig. 2).[33,34] To get further insights in the microcrystalline structure, a refinement based on an isotropic model (Le Bail method) has been performed, leading to the determination of the unit cell parameters and the estimation of the crystallite sizes for each sample (Table S1 and Fig. S1). The refinement indicates that the Mo_2C-AHM sample crystallizes in the orthorhombic system with space group *Pbcn*, and exhibits unit–cell parameters of $a = 4.747(1)$ Å, $b = 6.004(2)$ Å, and $c = 5.196(1)$ Å. The average crystallite size is approximately 14.3(1) nm. The two other materials crystallize similarly. For the Mo_2C-HMC sample, the unit–cell parameters are $a = 4.726(1)$ Å, $b = 6.015(3)$ Å, and c

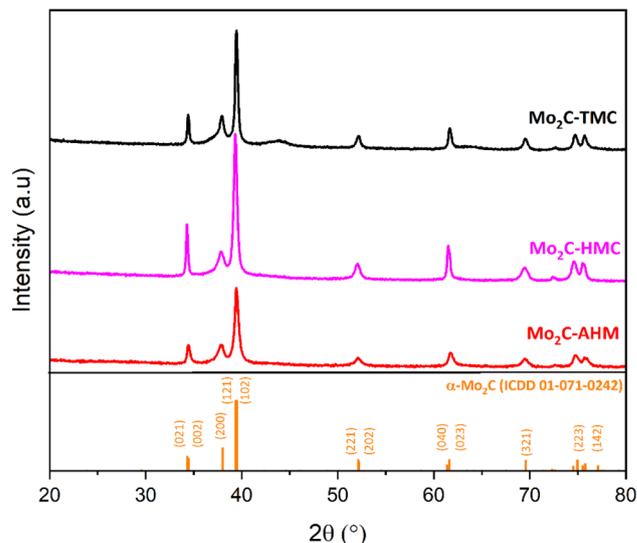**Fig. 2** Powder-XRD patterns of Mo_2C-TMC (black line), Mo_2C-HMC (magenta line) and Mo_2C-AHM (red line).

$= 5.198(1)$ Å. The Mo_2C-TMC sample shows lattice parameters of $a = 4.741(1)$ Å, $b = 6.015(2)$ Å, and $c = 5.205(1)$ Å. The average crystallite sizes for the Mo_2C-HMC and Mo_2C-TMC samples are 30.3(1) nm and 26.9(1) nm, respectively. All samples exhibit an average crystallite size within the nanometer range (Table 1). Notably, the synthesis method and in particular the choice of the starting precursor slightly influences the value of the unit cell parameters (Fig. S1 and Table S1).

Elemental analyses and determination of the specific surface area (SSA) through BET measurements were carried out for the three materials. As shown in Table 1, the use of cluster-based precursors leads to materials with significantly higher SSA; SSA are equal to 103 m^2 g^{-1} for the Mo_2C-TMC and 318 m^2 g^{-1} for Mo_2C-HMC compared to SSA = 33.1 m^2 g^{-1} for Mo_2C-AHM. Worth is noticing that the SSA of the AHM-derived sample reported here is also much higher than those reported by Vitale *et al.*[25] However, the new synthesis routes reported in this work also result in notably higher carbon contents (TMC: %$_{wt}$ C = 17.1%, HMC: %$_{wt}$ C = 31.1%) compared to the AHM route (%$_{wt}$ C = 5.9%), the later matches the calculated carbon content in Mo_2C. The carbon content for the different materials scales with the SSA values, suggesting that the residual amorphous carbon contributes to the increase of SSA values. Raman experiments confirmed the presence of amorphous carbon, exhibiting a high graphitization degree for the three compounds as indicated by the low values of the intensity I_D/I_G ratio (Fig. S2). This aspect is important in terms of electrocatalytic applications because the catalytic efficiency of an electrocatalyst is affected by its electric conductivity. A poor conductivity leads to large overpotentials. Graphitic carbon helps in improving the electrical conductivity. On the other hand, the samples prepared from cluster-based precursors exhibit significant oxygen contents, notably the Mo_2C-TMC compounds, in relation to the different synthesis modes used. A very small amount of nitrogen is detected for Mo_2C-TMC and Mo_2C-AHM due to the presence of

11334 | *J. Mater. Chem. A*, 2026, **14**, 11332–11343

This journal is © The Royal Society of Chemistry 2026

Table 1 Averaged crystallites size, elemental analyses and specific surface areas of Mo$_2$C-TMC, Mo$_2$C-HMC and Mo$_2$C-AHM synthesized through the sucrose route

Molybdenum precursor	Temperature (°C)	Rietveld crystallite sizes (nm)	TEM crystal sizes (nm)	%wt (N)	%wt (C)	%wt (O)	SSA (m^2 g^{-1})
[(NH$_4$)$_6$Mo$_7$O$_{24}$·4H$_2$O] AHM	700	14.3 ± 0.1	20–25	1.2 ± 0.5	5.9 ± 0.5	6.8 ± 0.5	33.1 ± 0.2
(TBA)$_2$Mo$_6$Cl$_{14}$ TMC	625	26.9 ± 0.1	20	1.2 ± 0.5	17.1 ± 0.5	14.6 ± 0.5	103 ± 15
(H$_3$O)$_2$Mo$_6$Cl$_{14}$ HMC	625	30.3 ± 0.1	Needles 50–100 length, diam. few nm —		31.1 ± 0.5	5.3 ± 0.5	318 ± 15

tetrabutylammonium or ammonium cations in the corresponding Mo precursors.

The morphology of the crystallites of Mo$_2$C-TMC, Mo$_2$C-HMC and Mo$_2$C-AHM powders were further characterized by scanning electron microscopy (SEM) and transmission electron microscopy (TEM)(Fig. 3). Fig. 3a–c shows SEM images of the Mo$_2$C-AHM, Mo$_2$C-HMC, and Mo$_2$C-TMC materials. In all three images, the particles appear aggregated with highly porous surfaces. In the case of the Mo$_2$C-AHM sample (Fig. 3a), the size aggregates range from approximately 0.5 to 1 μm. For the Mo$_2$C-HMC sample (Fig. 3b), a distinctive bimodal distribution is observed, consisting of large aggregates (~10 μm) intermixed with smaller ones (<0.5 μm). The Mo$_2$C-TMC sample (Fig. 3c) appears to be highly porous, with the presence of very fine nanoparticles (of 10 nm range) surrounding significantly larger particles (>1 μm). TEM image shows that the α-Mo$_2$C

synthesized via the AHM route consists of aggregated, roughly spherical nanocrystals with diameters ranging from 20 to 25 nm (Fig. 3d, and S4). In contrast, the Mo$_2$C-HMC exhibits needle-like particles with lengths between 50 and 100 nm and diameters of only a few nanometers (Fig. 3e). These needles are surrounded by smaller aggregated nanoparticles. For the Mo$_2$C-TMC sample, the nanocrystals appear highly aggregated, making it difficult to precisely determine their dimensions. However, an estimated size is on the order of 20 nm (Fig. 3f). Energy-dispersive X-ray spectroscopy (EDS) analysis confirms the presence of Mo alongside with a large amount of carbon (Fig. S3). The SAED (Selected Area Electron Diffraction) patterns of the Mo$_2$C-AHM, Mo$_2$C-HMC, and Mo$_2$C-TMC samples are displayed in Fig. 3g–i, respectively. The diffraction rings observed in all three patterns confirm the formation of α-Mo$_2$C. The measured interplanar spacings (Fig. S5) correspond to the
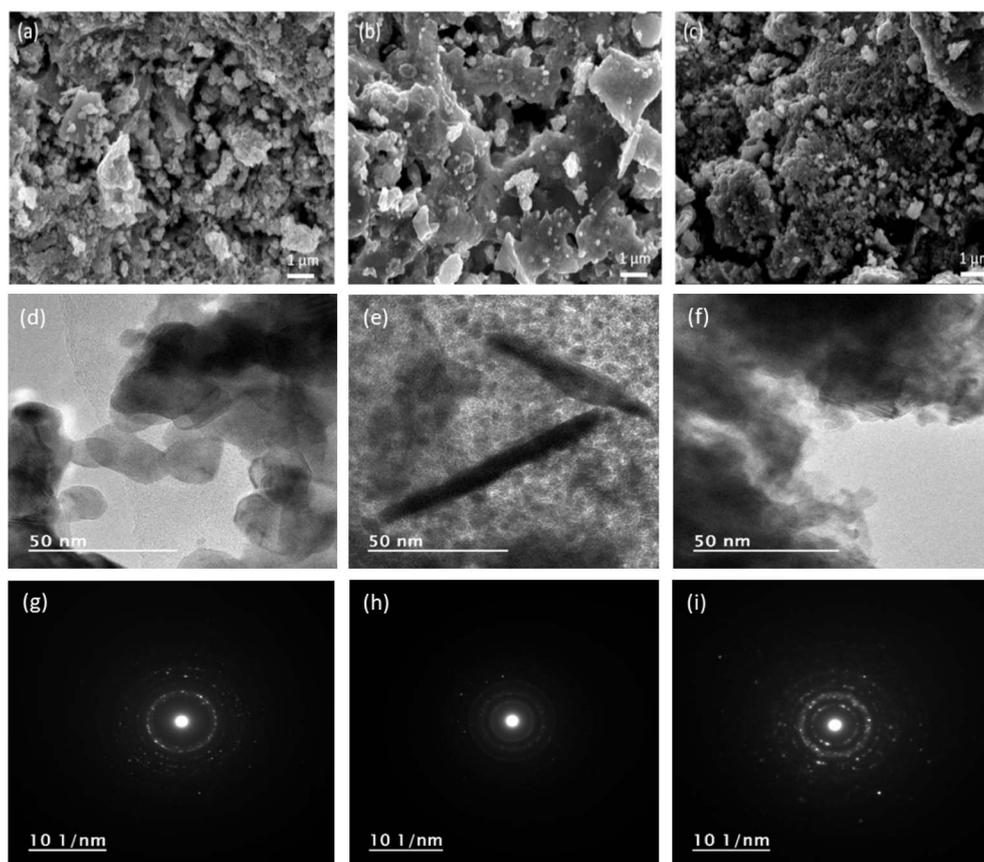
Fig. 3 (a–c) SEM images for Mo$_2$C-AHM (a), Mo$_2$C-HMC (b) and Mo$_2$C-TMC (c). (d–f) TEM images for Mo$_2$C-AHM (d), Mo$_2$C-HMC (e) and Mo$_2$C-TMC (f). (g–i) SAED patterns of Mo$_2$C-AHM (g), Mo$_2$C-HMC (h) and Mo$_2$C-TMC (i).

This journal is © The Royal Society of Chemistry 2026

J. Mater. Chem. A, 2026, 14, 11332–11343 | 11335

(021), (200), (121), and (221) planes of the orthorhombic α-Mo$_2$C phase (space group *Pbcn*). Notably, the SAED pattern of the Mo$_2$C-HMC sample (Fig. 3h) exhibits diffuse diffraction rings, suggesting lower crystallinity and smaller crystallite size in this sample. In addition, both the Mo$_2$C-HMC and Mo$_2$C-TMC samples show an extra diffraction ring (Fig. S5) that may correspond to the (−111) plane of the monoclinic MoO$_2$ phase (space group *P*2$_1$/*c*). However, no corresponding diffraction peaks of MoO$_2$ are detected in the XRD patterns of these samples (Fig. 1), indicating that the amount of MoO$_2$ is likely below the detection limit of the XRD technique.

X-ray photoelectron spectroscopy (XPS) analyses were further performed to probe in detail the chemical composition of the outermost surface of the materials (probing depth 5–10 nm). Moreover, XPS also allows investigation of amorphous parts of the materials in contrast to XRD. Survey spectra recorded for the 3 samples show the photoelectron peaks from the elemental species Mo, C and O (Fig. S6). Further information regarding the chemical states of the different species could be derived through the peak-fitting of the high-resolution core level spectra in the Mo 3d regions (Fig. 4). Spectra in the Mo 3d display the characteristic doublet peak structures Mo 3d$_{5/2}$ and Mo 3d$_{3/2}$ due to spin orbit splitting with an energy separation equal to 3.1 eV. The decomposition of the Mo 3d signal with 4 pairs of doublets reveals contributions of four redox states (+2, +3, +4 and +6) for Mo on the surface; +3 and +4 states may be due to surface defects. The Mo^{4+} at 231.9 ± 0.2 eV (3d$_{5/2}$) and Mo^{6+} at 232.9 ± 0.2 eV (3d$_{5/2}$) species are attributed to MoO$_2$ and MoO$_3$ species, respectively. While this observation falls in line with the analysis of the SAED patterns, it should also be mentioned that these species are very often observed when the carbides are exposed to air.[35,36] Low-valence states are more interesting to focus on because they are known to be much more active towards HER. Mo^{2+} at 228.6 ± 0.2 eV could be attributed to Mo in Mo$_2$C while Mo^{3+} at 229.6 ± 0.2 eV prevails in MoC$_y$ species.[37–39] From the atomic ratio in the Mo^{2+} and Mo^{3+} decompositions of the Mo 3d signal, we could derive an overall stoichiometry for Mo$_x$C species (Table S2), indicating the coexistence of α-Mo$_2$C with amorphous MoC$_y$ species. The origin and the precise nature and location of the MoC$_y$ species cannot be unambiguously determined from the present data. Possible explanations involve either the presence of an amorphous MoC$_y$ phase or the development of a carbon-rich shell around the α-Mo$_2$C crystallites, displaying intermediate structural characteristics.

It is further interesting to compare the Mo^{2+}/Mo^{3+} atomic ratio within the series of the 3 materials. It could be seen that the surface composition of Mo$_2$C-TMC has much more Mo^{2+} than Mo$_2$C-HMC and Mo$_2$C-AHM. Even if all 3 materials consist of α-Mo$_2$C in the bulk as revealed by the XRD analysis, the presence of amorphous MoC$_y$ as secondary phase and/or at the α-Mo$_2$C particles surfaces (or at the bulk surfaces) will have a strong impact on the electrocatalytic process, which occurs at the material surface, since the electronic densities at the Mo^{2+} and Mo^{3+} sites are different. Higher content of MoC$_y$ in Mo$_2$C-AHM is probably related to the +6-oxidation state of Mo in AHM. Hence, α-Mo$_2$C is known as an efficient HER
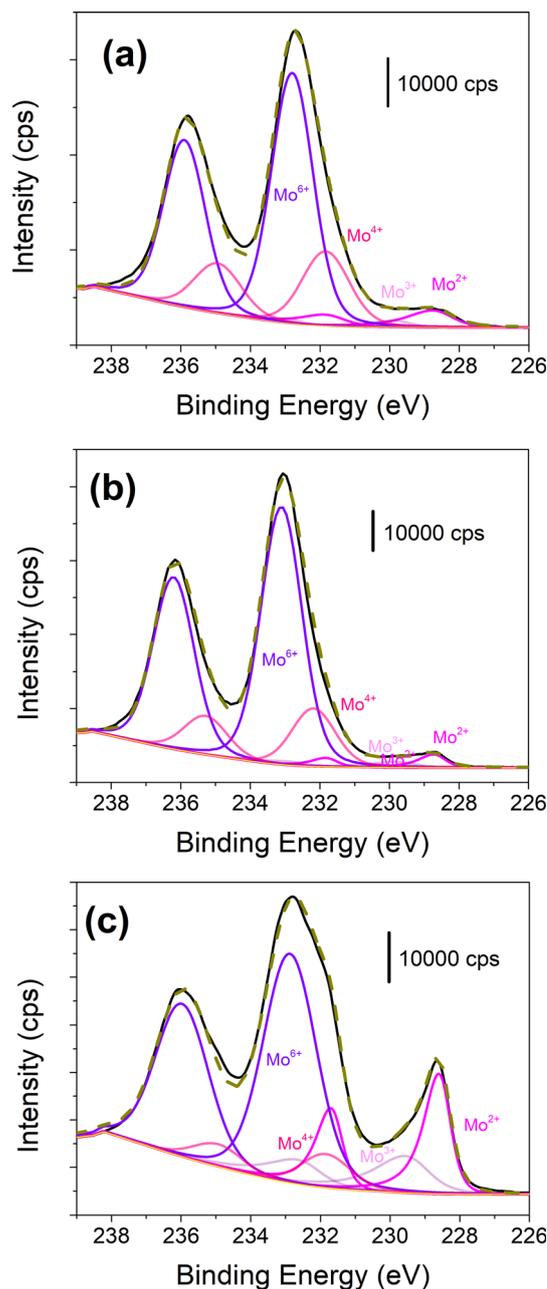

Fig. 4 High resolution core level XPS spectra in the Mo 3d region for Mo$_2$C-TMC (a), Mo$_2$C-HMC (b) and Mo$_2$C-AHM (c).

electrocatalyst owing to a strong hydrogen binding energy while weak or inefficient hydrogen adsorption in MoC$_y$ restricts its HER activity.[40–42] However, the coexistence of amorphous MoC$_y$ at low content with α-Mo$_2$C is likely to favor good HER performance.

2.2. Electrocatalytic HER performance

The HER activities of Mo$_2$C-TMC, Mo$_2$C-HMC and Mo$_2$C-AHM were investigated in aqueous 1 M KOH by linear sweep voltammetry (LSV). Fig. 5a presents the polarization curves of the 3 materials deposited onto the rotating disk electrode (RDE) as an ink with a classical carbon black support (Vulcan XC 72) at a low
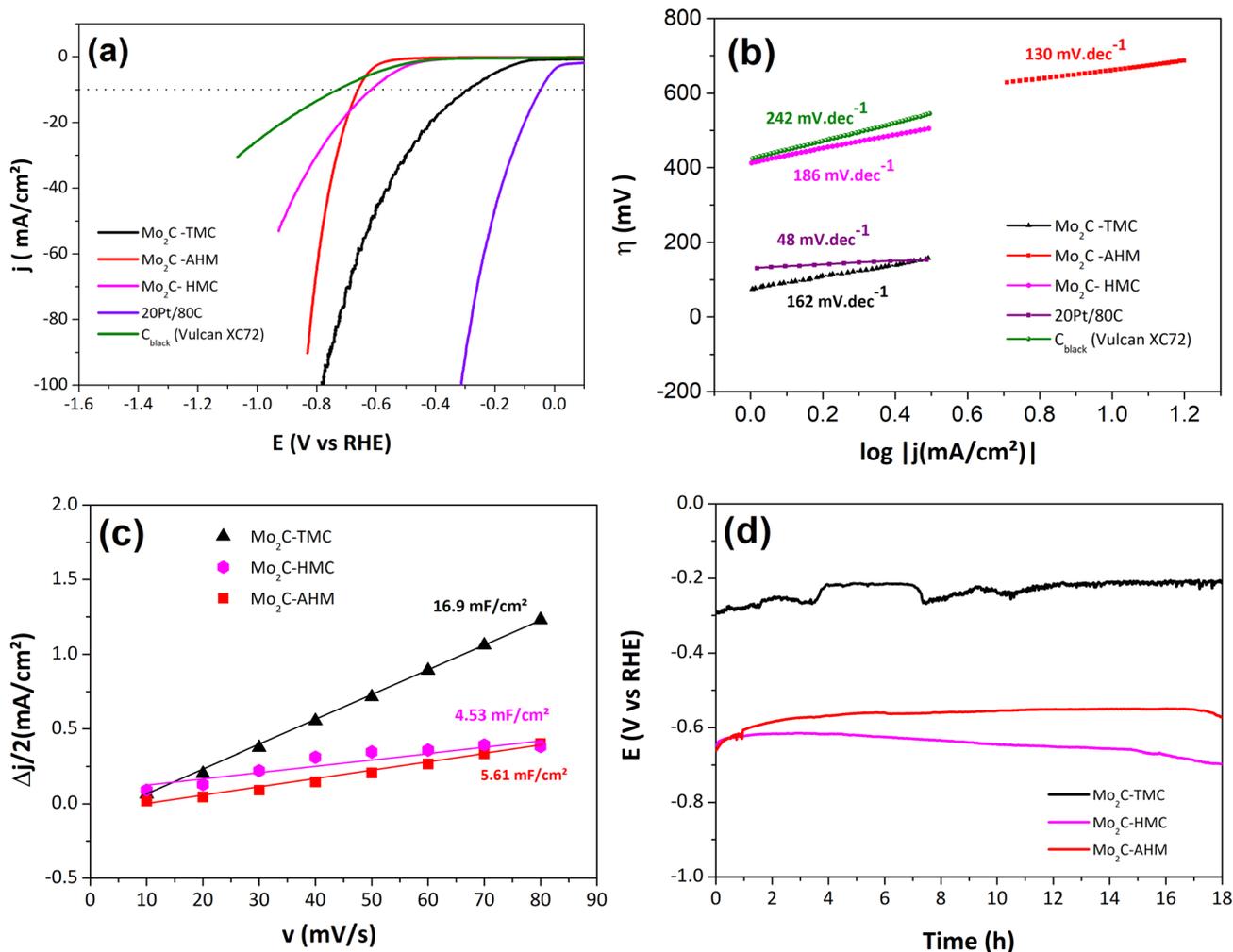
11336 | *J. Mater. Chem. A*, 2026, **14**, 11332–11343

This journal is © The Royal Society of Chemistry 2026

Fig. 5 (a) *iR*-Corrected HER polarization curves in aqueous 1 M KOH at 10 mV s^{-1} for Mo$_2$C-TMC (black line), Mo$_2$C-HMC (magenta line), Mo$_2$C-AHM (red line), carbon support (green line) compared to benchmark Pt/C (violet line) (b) corresponding Tafel slopes, (c) $\Delta J/2$ *vs. v* plots where Δj is the difference between anodic and cathodic capacitive current density derived from cyclic voltammetries used for determining the C_{dl} values (see SI) (d) chronopotentiometry at applied current density $j = -10$ mA cm^{-2} for deposits of Mo$_2$C-TMC, Mo$_2$C-HMC and Mo$_2$C-AHM.

mass loading (150 μg cm^{-2}). As a reference, the commercially available benchmark Pt/C catalyst with the same mass loading was also measured while the voltammetric response of carbon support alone is also recorded for comparison purposes. All the 3 Mo carbide materials unambiguously exhibit HER activity when compared to carbon support alone.

Among the Mo carbides materials, Mo$_2$C-TMC exhibits the highest HER activity as supported by the lowest onset potential of 86 mV *vs.* RHE (set arbitrarily at 1 mA cm^{-2}) and the lowest *iR*-corrected overpotential value at -10 mA cm^{-2}, $\eta_{10} = 296$ mV (Table 2), although the Mo$_2$C-AHM activity can compete at large current density. Yet, the η_{10} value is expectedly far higher than that of benchmarked Pt. The Tafel slopes at low overpotentials for the 3 Mo carbides materials are also significantly higher than that obtained for Pt/C, indicating a different mechanism for the HER process. The values of the Tafel slopes depend on the rate-determining step (rds) for the electrochemical process. A value equal or close to 120 mV dec^{-1} indicates that the HER is controlled by the Volmer reaction step which involves the

electrochemical adsorption of hydrogen atom onto the catalytic sites. A slope of 40 mV dec^{-1} is obtained when the rds is the electrochemical desorption (Heyrovsky mechanism). A value of 48 mV dec^{-1} was found for the Pt/C reference, suggesting a mixed Volmer–Heyrovsky mechanism, which is consistent for Pt under alkaline conditions.[43,44] All three Mo-based materials show Tafel slopes larger than 120 mV dec^{-1}, suggesting a less efficient HER process than for a platinum-based catalyst and involving a Volmer limiting mechanism.

In Fig. 5c, we have plotted the capacitive current density ($\Delta j/2$) against the sweep rate (Fig. S7a, 8a, and 9a), which allows determination of C_{dl} values. The electrochemically active surface area (S_{ECSA}) is also an important metric for assessing catalytic activity and ais proportional to the C_{dl} values. Among the studied materials, the Mo$_2$C-TMC exhibits the highest C_{dl} value (16.9 mF cm^{-2}) against 4.5 and 5.6 mF cm^{-2} for Mo$_2$C-HMC and Mo$_2$C-AHM, respectively.

In order to examine the long-term stability of the Mo$_2$C molybdenum carbides as HER electrocatalysts,

Table 2 Overpotentials at −10 mA cm^{-2} (denoted η_{10}), S_{ECSA} values and R_{CT} values calculated for the various undoped Mo$_2$C studied before and after 18 hours chronoamperometry (after CP), compared with platinum and carbon support

	η_{10} (mV)	η_{10} (mV) after CP[a]	Tafel slopes (mV dec^{-1})	Tafel slopes (mV dec^{-1}) after CP	C_{dl} (mF cm^{-2})	C_{dl} (mF cm^{-2}) after CP	R_{CT} (Ω)
Mo$_2$C-TMC	296	212	162	95	16.9	22.1	65 ± 1
Mo$_2$C-HMC	618	321	186	103	4.5	3.1	75 ± 1
Mo$_2$C-AHM	662	408	130	118	5.6	3.3	230 ± 1
Pt/C	48	—	48	—	—	—	—
Carbon support	732	—	242	—	—	—	—

[a] Chronopotentiometry at applied current density equal to −10 mA cm^{-2} for 18 h in 1 M KOH.

chronopotentiometry measurements were conducted over 18 hours at an applied current density of −10 mA cm^{-2} (Fig. 5d). The potential responses exhibit periodic fluctuations, which can be attributed to the intermittent formation and detachment of hydrogen gas bubbles on the surface of the working electrode. Interestingly, the measured potentials become less negative over time, and this observation is more marked for Mo$_2$C-TMC and Mo$_2$C-AHM than for Mo$_2$C-HMC. Such a behavior may result from electrochemical surface restructuring or improved electrolyte wetting of the porous structure, suggesting activation of the materials under operation.

To further confirm these activation phenomena, polarization curves, Tafel plots, capacitive $\Delta j/2$ *vs.* ν plots (Fig. S7b, 8b, and 9b) were recorded after 18 hours-chronopotentiometry (Fig. 6a–c).

The post-stability polarization curves reveal a marked enhancement in the electrocatalytic performance of all materials (Fig. 6a, and S10). The activities of the 3 catalytic materials
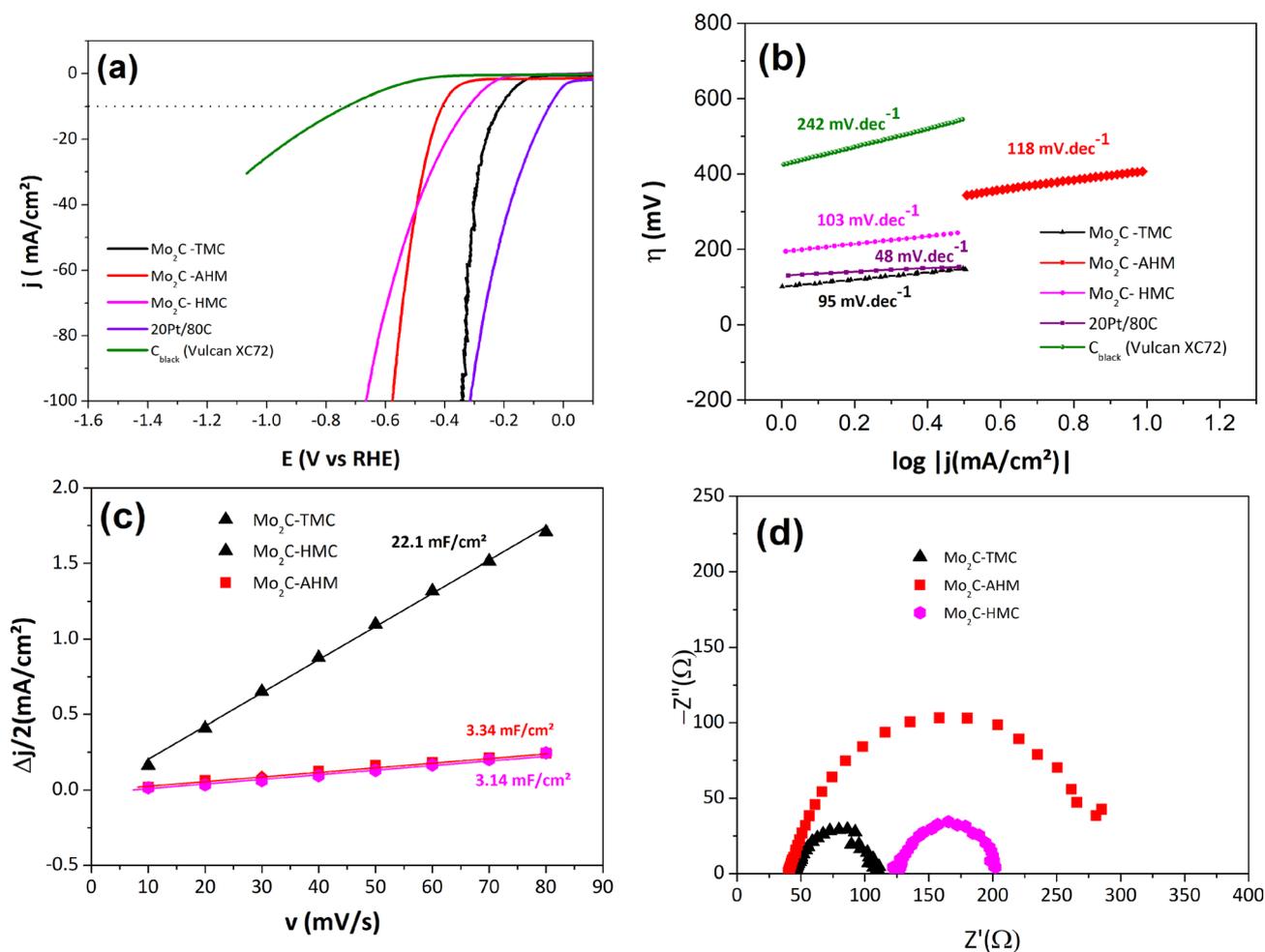

Fig. 6 (a) *iR*-Corrected HER polarization curves in aqueous 1 M KOH at 10 mV s^{-1} for Mo$_2$C-TMC (black line), Mo$_2$C-HMC (magenta line), Mo$_2$C-AHM (red line) after 18 h-chronopotentiometry, compared to carbon support (green line) and benchmark Pt/C (violet line) (b) corresponding Tafel slopes, (c) $\Delta J/2$ *vs.* ν plots (d) EIS Nyquist plots for the 3 materials.

11338 | *J. Mater. Chem. A*, 2026, **14**, 11332–11343

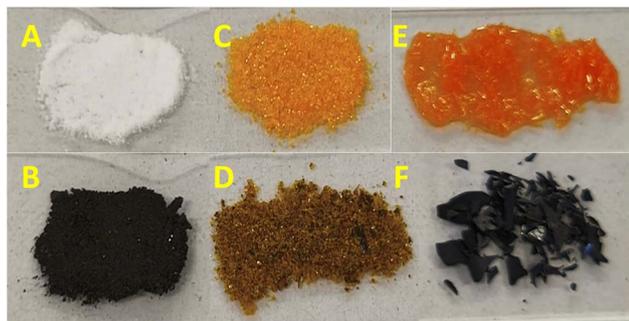This journal is © The Royal Society of Chemistry 2026

Fig. 7 Images of powdered samples of (A) AHM starting precursor, (B) AHM + sucrose before carburization, (C) TMC starting precursor, (D) TMC + sucrose before carburization, (E) HMC precursor, (F) HMC + sucrose before carburization.

are also represented against normalization with approximated ECSA values and with mass (mass activity) for comparison purposes (Fig. S11 and S12). Mo_2C-TMC still shows the highest performance with a significantly reduced overpotential by more than 80 mV at $j = -10$ mA cm^{-2}, $\eta_{10} = 212$ mV (Table 2). Similarly, Mo_2C-HMC and Mo_2C-AHM exhibit improved η_{10} values, being equal to 321 mV and 408 mV, respectively (Table 2). These findings are further supported by the Tafel slope values presented in Fig. 6b. After an 18 h-chronopotentiometry, all Mo_2C catalysts display lower Tafel slopes, probably due to enhanced process kinetics. Notably, a slope equal to 95 mV dec^{-1} is obtained for Mo_2C-TMC, being the lowest among the three compounds and the closest to that of Pt/C, suggesting that the HER is similarly controlled by a mixed Heyrovsky–Volmer mechanism for both Pt/C and Mo_2C-TMC. The superior activity of Mo_2C-TMC is also confirmed by an increase in its C_{dl} value, hence of the ECSA value, in contrast to the two other materials for which slightly lower values are obtained (Fig. 6c). At this stage we do not have a clear-cut explanation concerning the activation of the catalysts after the chronopotentiometry. As noted above, the activation may result from electrochemical restructuring leading to more active catalytic sites and/or to better wetting properties for the electrolyte. We may also postulate a reductive removal of the surface oxides MoO_2 and especially MoO_3 through the galvanostatic electrolysis since this has been reported earlier.[36]

Additionally, electrochemical impedance spectroscopy (EIS) measurements were performed for a current density above -10 mA cm^{-2}, *i.e.* at overpotentials of 296 mV, 618 mV, and 662 mV for Mo_2C-TMC, Mo_2C-HMC, and Mo_2C-AHM, respectively, before the stability tests. The data are shown according to Nyquist diagrams by plotting the imaginary part of the impedance $(-Z'')$ against the real part (Z') of the complex impedance $(Z = Z' + iZ'')$ as a function of frequency (Fig. 6d). The corresponding Nyquist plots show well-defined semicircles that can be modeled using a Randles equivalent circuit comprising resistance (cell resistance R_s) in series with the charge transfer resistance (R_{CT}) and a constant phase element (CPE) in parallel. In this model, the diameter of the semicircle along the Z' axis corresponds to the charge transfer resistance R_{CT}. Consistent

with the other electrochemical data, the R_{CT} of Mo_2C-TMC ($R_{CT} = 65 \pm 1\ \Omega$) is found to be smaller than those determined for Mo_2C-HMC ($R_{CT} = 75 \pm 1\ \Omega$) and Mo_2C-AHM ($R_{CT} = 230 \pm 1\ \Omega$), confirming faster charge-transfer kinetics for HER for Mo_2C-TMC. Worth is outlining the strong difference for R_{CT} values for the two materials synthesized from the cluster routes compared to the classical route. This observation agrees well with the larger content of residual graphitized carbon which should enhance the electrical conductivity and hence facilitates the charge transfer.

Among the 3 α-Mo_2C carbides, the Mo_2C-TMC catalyst consistently demonstrates superior performance, with the lowest η_{10} and Tafel slope, highest C_{dl}, and lowest charge transfer resistance (R_{CT}). Its HER performance competes well with other reported Mo carbides materials (Table S3), especially when considering the low charge loading which is herein used. It is attributed to its high specific surface area, large surface porosity, in line with the small crystallite sizes (*ca.* 30 nm), the presence of residual carbon sp^2 and a larger Mo^{2+} species content (Table S2). In contrast, Mo_2C-HMC, despite having a higher surface area (*ca.* 300 m^2 g^{-1}) and similar crystallite sizes, shows poorer HER activity than Mo_2C-TMC, due to the lower content of Mo^{2+} species at the material surface (Table S2). Meanwhile, the Mo_2C-AHM sample, though featuring smaller crystallite sizes, presents a lower specific surface area and an even weaker HER activity than Mo_2C-HMC. These findings highlight the critical balance between material structure/morphology and surface composition for tuning the catalytic efficiency of α-Mo_2C-based materials.

3. Conclusion

In summary, we have developed a new strategy for the synthesis of α-Mo_2C-based carbides powder materials by combining a biosourced carbon with Mo_6-based cluster precursors to take advantage of their nanostructured properties. The use of the Mo-clusters as Mo source enables carburization at relatively low temperature, similar to the case of the AHM heptamolybdate nanosized based precursor. The resulting materials display superior physicochemical properties compared to those obtained *via* the already reported AHM route, including higher specific surface area, smaller crystallite size, and enhanced surface porosity. This improvement can be related to the +2-oxidation state of Mo in the Mo_6 cluster-based precursors, which is consistent with that of the targeted α-Mo_2C, in contrast to the +6-oxidation state of Mo in the heptamolybdate. The α-Mo_2C-based carbide synthesized through the use of cluster-based precursors demonstrates superior performance as electrocatalyst for the hydrogen evolution reaction (HER) compared to those prepared using AHM. Moreover, the catalyst derived from TMC shows superior performance relative to that obtained from HMC, emphasizing the decisive influence of the counter-cations in the cluster precursor. These cations govern not only precursor solubility but also the intrinsic carbon content available during carburization. In particular, the tetra-butylammonium ions in TMC provide a substantial carbon contribution (24.7 wt% of $((n\text{-}C_4H_9)_4N)_2[Mo_6Cl_{14}])$, promoting

a more homogeneous distribution of carbon and molybdenum and facilitating the formation of α-Mo$_2$C crystallites with limited surface oxidation.

Specifically, the Mo$_2$C-TMC catalyst shows improved electrocatalytic performance at low catalyst loading in alkaline media with the highest η_{10}, larger ECSA, lowest Tafel slope and charge transfer resistance, outperforming the other carbides synthesized in this study and showing comparable or even better efficiency to several materials as reported in the literature (Table S3). Moreover, a 18 h-chronopotentiometry followed by electrochemical analyses reveals that the Mo$_2$C-TMC catalyst undergoes activation after operation at -10 mA cm^{-2}, leading to improved HER performance.

Although nanostructuring is widely recognized as a crucial factor in achieving high electrocatalytic performance for HER, this work indicates that no simple correlation exists in the case of α-Mo$_2$C carbide. On the contrary, they emphasize the need to balance key structural and morphological parameters and the chemical composition of the crystallite surface, all of which are strongly influenced by the synthesis route and precursor choice. For optimal performance, the α-Mo$_2$C-based catalyst must integrate the physicochemical features of α-Mo$_2$C—such as high specific surface area, significant porosity, and small crystallite size—with the presence of crystalline domains and a suitable surface chemistry, characterized by minimal residual MoC$_y$ and the presence of graphitized carbon. The latter, formed during synthesis, contribute to improving the electrical conductivity by lowering charge-transfer resistance.

Looking ahead, further optimization of the precursor design and synthesis parameters could enable precise control over the surface chemistry and defect structure of α-Mo$_2$C, thereby enhancing its catalytic activity and durability. In particular, tailoring the interplay between nanostructure, composition, and electronic properties, offers promising pathways to develop α-Mo$_2$C-based catalysts that can compete with noble metals for HER.

4. Experimental section

4.1. Chemicals

Ammonium heptamolybdate tetrahydrated was obtained from ACROS (99+%) and sucrose, ACS from Alfa Aesar. Nafion® 117 binder, 20% platinum on graphitized carbon (Pt/C) were purchased from Sigma-Aldrich. Carbon black acetylene was from Alfa Aesar and VULCAN Carbon black from Cabot Corp. KOH of analytical grade was purchased from Fisher Scientific. All Chemicals were used as received. Ultrapure water (Veolia Water-STI) with a resistivity of 18.2 MΩ was employed in the preparation of the aqueous solutions.

4.2. Syntheses of Mo carbides catalysts

4.2.1 AHM route. 1 g (8.1×10^{-4} mol) of ammonium heptamolybdate tetrahydrate [(NH$_4$)$_6$Mo$_7$O$_{24}$·4H$_2$O] (1235 g mol^{-1}/CAS no. 12054-85-2) was dissolved in 10 mL of distilled water. The molybdenum content in AHM is 54.33 wt%, corresponding to 0.5433 g (5.66×10^{-3} mol) in 1 g of compound.

Separately, 0.3296 mg (9.63×10^{-4} mol) of sucrose (C$_{12}$H$_{22}$O$_{11}$) was dissolved in a minimum amount of water in order to obtain a C/Mo ratio of 2. The amount of carbon in sucrose is 42.1 wt%; corresponding to 0.1388 g (11.5×10^{-3} mol). The sucrose solution was then added to the AHM solution under magnetic stirring for 20 minutes at room temperature. The resulting homogeneous solution was then evaporated in an oven at 100 °C for 24 hours yielding a dried solid product. After grinding in an agate mortar, a fine black powder was obtained. As shown in Fig. 7, the color changes drastically from white (AHM) to black (dried AHM + sucrose mixture). The comparison between the X-ray powder pattern of AHM and that of the grounded solid-state product (AHM + sucrose) obtained after treatment at 100 °C during 24 h reveals that the mixture is amorphous, although four distinguishable diffraction peaks are observed (Fig. S13). They do not correspond to diffraction peaks of the starting AHM. The SEM analysis showed that the powder consists of micrometric matter aggregates of poorly defined shaped (Fig. S14). This fine powder was then treated at 700 °C for 24 hours (10 °C min^{-1}) in a 5% H$_2$/Ar atmosphere to obtain the AHM product. Note that the difference between the protocol reported by Vitale and that reported herein, is that Vitale et al.[25] did not use a hydrogenated gas flow.

4.2.2 TMC route. 455 mg (2.92×10^{-4} mole) of ((nC$_4$H$_9$)$_4$-N)$_2$Mo$_6$Cl$_{14}$ precursor (TMC – 1556.9 g mol^{-1}) were dissolved in 20 mL of acetone. The molybdenum content in ((nC$_4$H$_9$)$_4$-N)$_2$Mo$_6$Cl$_{14}$ is 36.97 wt% (0.168 g, 1.75×10^{-3} mol), while that of carbon is 24.68 wt% (0.112 g, 9.3×10^{-3} mol). Separately, 150 mg of sucrose (0.063 g of carbon, 5.2×10^{-3} mol) was dissolved in water. This amount of sucrose corresponds to the necessary quantity to obtain a C/Mo molar ratio of 3, not accounting for the amount of carbon already present in TMC. This sucrose solution was then added to the TMC solution under magnetic stirring. Considering that the intrinsic C/Mo ratio in TMC is 5.31, the overall C/Mo molar ratio in the TMC + sucrose mixture is 8.3. The acetone/water mixture was stirred and heated at 55 °C for 20 minutes until a homogeneous solution was obtained. The solvents were then evaporated in an oven at 100 °C for 24 hours until obtaining a dried solid-state product. As shown in Fig. 7, the visual appearance of the mixture before grinding contrasts with that of the starting TMC. The comparisons of the X-ray powder pattern of the starting TMC with that of the mixture (TMC + sucrose) after heating at 100 °C evidence that the TMC structure remains intact after treatment (Fig. S15). SEM/EDS investigations revealed the presence of well-defined crystals of TMC embedded in an organic matrix, indicating that no pre-reactions occurred at this stage (Fig. S14). The dried product was ground resulting in an orange-brownish colored fine powder that was then heated at 625 °C for 24 hours (heating rate: 5 °C min^{-1}) under a 5% H$_2$/Ar atmosphere.

4.2.3 HMC route. 730 mg (5.9×10^{-4} mol) of (H$_3$O)$_2$Mo$_6$-Cl$_{14}$·7H$_2$O (1236 g mol^{-1}) was dissolved in 20 mL of absolute ethanol. The molybdenum content in HMC is 46.6 wt%, corresponding to 0.3399 g (3.54×10^{-4} mol). A total of 300 mg of sucrose (0.12633 g of C, 10.4×10^{-3} mol) was dissolved in a minimal amount of water and added to the solution of HMC

11340 | J. Mater. Chem. A, 2026, 14, 11332–11343

This journal is © The Royal Society of Chemistry 2026

(C/Mo molar ratio = 3) under magnetic stirring at 55 °C. After complete homogenization, the solvent was evaporated at 100 °C for 24 hours until obtaining a solid-state product. As shown in Fig. 7, a drastic change of color from orange to black is observed between the HMC precursor and the mixture (HMC + sucrose) after heating at 100 °C. The analysis of the X-ray powder patterns of the starting HMC with that of the mixture (HMC + sucrose) heated at 100 °C evidences a total amorphization of the HMC phase (Fig. S16). SEM analyses revealed that the solid-state obtained by heating at 100 °C for 24 h is composed of homogeneous smooth matter aggregates (Fig. S14). The chemical composition determined by EDS analyses revealed no evolution of the with Cl/Mo between starting HMC and the (HMC + sucrose) mixture after heating at 100 °C. It seems that cluster units are fixed in an organic carbon matrix without decomposition of the cluster. The resulting black solid is ground and subjected to the same heat treatment as for the TMC sample (625 °C for 24 hours under 5% H$_2$/Ar, 5 °C min^{-1}).

4.3. Instrumentation

X-ray diffraction (XRD) patterns were recorded in the 2θ range of 20–80° using a PANalytical X'PERT powder diffractometer equipped with a Cu Kα radiation source (K$_{\alpha 1}$ (1.54056 Å) et K$_{\alpha 2}$ (1.54439 Å), 40 kV, 40 mA) and a PIXcel 1D detector. Phase identification was carried out using the HighScore Plus software package. Structural refinement of the diffraction data was performed by the LeBail method using the FullProf Suite software. Elemental analysis was performed to measure Nitrogen, Oxygen and carbon mass percentage content (%N, %C, %O). %N and %O were determined using a LECO TC-600 analyzer through the inert gas fusion method. Nitrogen was quantified as N$_2$ by thermal conductivity detection, while oxygen was measured as CO$_2$ by infrared detection. The instrument was calibrated using certified LECO standards. Although factors such as water contamination, adsorbed species, or the presence of high specific surface area powders can significantly affect analytical accuracy, the hot extraction technique employed here is recognized as one of the most reliable and rapid method for determining nitrogen and oxygen contents.[45] Carbon content was analyzed separately using a Thermo FlashSmart Elemental Analyzer. Carbon was oxidized and quantified as CO$_2$ using infrared detection. The specific surface area (SSA) was determined by using the Brunauer–Emmett–Teller (BET) method based on nitrogen physisorption measurements performed with a Micromeritics 3Flex analyzer. A N$_2$/He gas mixture (30%/70%) was used as the adsorptive. Prior to analysis, the samples were degassed under vacuum at 150 °C to remove adsorbed moisture and prevent surface hydration. Scanning electron microscopy (SEM) and chemical analysis were performed at the CMEBA (ScanMAT, Université de Rennes, France) using two JEOL instruments: a JSM-6301F for high-resolution imaging and a JSM-7100F equipped with energy-dispersive X-ray spectroscopy (EDS) detector for elemental analysis. TEM imaging was carried out using a JEOL-2100 microscope equipped with a LaB$_6$ electron source, operated at 200 kV. Elemental analysis was performed by Energy Dispersive X-ray Spectroscopy (EDS)

using an Oxford Instruments SDD 80 mm^2 detector. For sample preparation, a small quantity of molybdenum carbide powder was dispersed in absolute ethanol via ultrasonication, then deposited onto a copper grid coated with an elastic carbon film and dried under ambient conditions. XPS data have been collected by a NEXSA G2 (ThermoFischer Scientific) spectrometer using the Al Kα X-ray source working at 1486.6 eV and using a spot size of 200 µm^2. Survey spectra (0–1000 eV) were acquired with an analyzer pass energy of 200 eV (1 eV per step); high resolution spectra used a pass energy of 50 eV (0.1 eV per step). Binding energies were referenced to C 1s peak at 284.8 eV. The core level spectra were peak-fitted using the CasaXPS Software, Ltd. Version 2.3.25PR1.0. U 2 Tougaard background subtraction was used for the spectral analysis. Peaks were fitted with LA(50) function except Mo–C species which was fitted with Lorentzian asymmetyric, LA(1.2, 2.5, 30), function in the CasaXPS software. The peak areas were normalized by the manufacturer-supplied sensitivity factor (S$_{C\ 1s}$ = 1, S$_{Mo\ 3d}$ = 11.008, S$_{O\ 1s}$ = 2.88). For each sample, XPS survey spectra were recorded in three different locations, and we did not observe any difference. Raman spectra were collected using a confocal Raman spectrometer LabRAM HREvo (HORIBA Scientific) using a 532 nm laser directed on the sample through an objective (OLYMPUS, ×100 VIS LWD, N.A. 0.8). All measurements were carried out under ambient conditions at room temperature. Accumulation time for all samples is 120 s.

Electrochemical experiments were performed using an Autolab PGSTAT302N potentiostat-galvanostat (Metrohm), equipped with an impedance analyzer/AC frequency response analyzer (FRA), in a conventional three-electrode electrochemical cell. A DSA (MMO) and a Hg/HgO electrode in 1 M KOH (ALS) were used as counter and reference electrodes, respectively. A glassy carbon RDE (Origalys) of 3 mm diameter (geometric surface area = 0.0707 cm^2) on which the catalyst ink was deposited, was employed as the working electrode. All HER polarization curves were recorded by linear sweep voltammetry (LSV) at 10 mV s^{-1} in aqueous M KOH purged with Ar. The potentials were scaled against RHE by using the following equation

$$E_{RHE} = E_{Hg/HgO} + 0.059\ pH + E^0_{Hg/HgO}\ \text{with}\ E^0_{Hg/HgO} = +0.102\ V.$$

Electrochemical impedance spectroscopy (EIS) measurements were carried out at OCP for determining the ohmic drop or at an applied potential corresponding to $j = -10$ mA cm^{-2} over a frequency range from 100 kHz to 100 mHz at 10 mV amplitude. The ohmic drop was classically corrected with 95% iR correction using the automated function of the potentiostat. To calculate the double-layer capacitance (C_{dl}), cyclic voltammograms (CVs) were recorded in the non-faradaic region at different scan rates. C_{dl} (in mF cm^{-2}) corresponds to the slope of the $\Delta j/2$ vs. v plots where Δj is the difference between the anodic and cathodic charging current densities and v is the potential scan rate. The long-term stability of the catalytic electrodes was examined using chronopotentiometry at an applied −10 mA cm^{-2} current density for 18 h.

This journal is © The Royal Society of Chemistry 2026

J. Mater. Chem. A, 2026, **14**, 11332–11343 | **11341**

To prepare the catalyst ink, the amount of carbon support (Vulcan XC-72 with 5 wt% CBA) was adjusted according to the carbon content in the Mo_2C powders, so that the final inks contained 20 wt% catalyst and 80 wt% total carbon (including both the support and the carbon present in the synthesized materials). The mixture was suspended in 1 mL of isopropanol containing 40 μL of Nafion® solution (5 wt%) and subjected to ultrasonication for at least 30 minutes to ensure homogeneous dispersion. A 10 μL aliquot of the resulting ink was then drop-casted onto the glassy carbon disk of the RDE, then dried under ambient conditions for one night prior to any measurement.

Conflicts of interest

The authors declare no competing financial interest.

Data availability

The authors confirm that the data supporting the findings of this study are available within the article. As well as it will be shared on request.

Supplementary information (SI): detailed experimental data, characterization results (XRD, SEM, Raman, EDS, XPS), additional figures and tables on structural and electrochemical properties, and calculation methods. See DOI: https://doi.org/10.1039/d5ta09668e.

Acknowledgements

References

1 C. G. Morales-Guio, M. T. Mayer, A. Yella, S. D. Tilley, M. Grätzel and X. Hu, An Optically Transparent Iron Nickel Oxide Catalyst for Solar Water Splitting, *J. Am. Chem. Soc.*, 2015, **137**(31), 9927–9936.

2 M. G. Walter, E. L. Warren, J. R. McKone, S. W. Boettcher, Q. Mi, E. A. Santori and N. S. Lewis, Solar Water Splitting Cells, *Chem. Rev.*, 2010, **110**, 6446.

3 T. R. Cook, D. K. Dogutan, S. Y. Reece, Y. Surendranath, T. S. Teets and D. G. Nocera, Solar Energy Supply and Storage for the Legacy and Nonlegacy Worlds, *Chem. Rev.*, 2010, **110**, 6774.

4 Z.-Y. Yu, Y. Duan, X.-Y. Feng, X. Yu, M.-R. Gao and S.-H. Yu, Clean and Affordable Hydrogen Fuel from Alkaline Water Splitting: Past, Recent Progress and Future Prospects, *Adv. Mater.*, 2021, **33**, 2007100.

5 N. Sezer, S. Bayhan, U. Fesli and A. Sanfilippo, A Comprehensive Review of the State-of-the-Art of Proton Exchange Membrane Water Electrolysis, *Mater. Sci. Energy Technol.*, 2025, **8**, 44.

6 A. Carbone, S. C. Zignani, I. Gatto, S. Trocino and A. S. Aricò, Assessment of the FAA3-50 Polymer Electrolyte in Combination with a $NiMn_2O_4$ Anode Catalyst for Anion Exchange Membrane Water Electrolysis, *Int. J. Hydrogen Energy*, 2020, **45**, 9285.

7 T. F. Jaramillo, K. P. Jørgensen, J. Bonde, J. H. Nielsen, S. Horch and I. Chorkendorff, Identification of Active Edge Sites for Electrochemical H_2 Evolution from MoS_2 Nanocatalysts, *Science*, 2007, **317**, 100.

8 A. R. Zeradjanin, J.-P. Grote, G. Polymeros and K. J. J. Mayrhofer, A Critical Review on Hydrogen Evolution Electrocatalysis: Re-Exploring the Volcano-Relationship, *Electroanalysis*, 2016, **28**, 2256.

9 G. A. Blengini, D. Blagoeva, J. Dewulf, C. Torres de Matos, V. Nita, B. Vidal-Legaz, C. E. L. Latunussa, Y. Kayam, L. Talens Peiro, C. Baranzelli, S. Manfredi, L. Mancini, P. Nuss, A. Marmier, P. Alves-Dias, C. Pavel, E. Tzimas, F. Mathieux, D. Pennington, and C. Ciupagea, *Assessment of the Methodology for Establishing the EU List of Critical Raw Materials*, Publications Office of the European Union, Luxemburg, 2017, 978–92–79–69612–1.

10 Y. Xu, R. Wang, J. Wang, J. Li, T. Jiao and Z. Liu, Facile Fabrication of Molybdenum Compounds (Mo_2C, MoP and MoS_2) Nanoclusters Supported on N-Doped Reduced Graphene Oxide for Highly Efficient Hydrogen Evolution Reaction over Broad pH Range, *Chem. Eng. J.*, 2021, **417**, 129233.

11 Y. Ma, G. Guan, X. Hao, J. Cao and A. Abudula, Molybdenum Carbide as Alternative Catalyst for Hydrogen Production – A Review, *Renewable Sustainable Energy Rev.*, 2017, **75**, 1101.

12 C. Wan, Y. N. Regmi and B. M. Leonard, Multiple Phases of Molybdenum Carbide as Electrocatalysts for the Hydrogen Evolution Reaction, *Angew. Chem.*, 2014, **126**, 6525.

13 J. Li, J. Hu and P. Chen, Perspectives on Mo-based electrocatalysts for the hydrogen evolution reaction: a comprehensive review, *Energy Fuels*, 2023, **37**, 17803.

14 A. A. Feidenhans, Y. N. Regmi, C. Wei, D. Xia, J. Kibsgaard and A. King, Precious Metal Free Hydrogen Evolution Catalyst Design and Application, *Chem. Rev.*, 2024, **124**, 5617.

15 F. Dawood, M. Anda and G. M. Shafiullah, Hydrogen Production for Energy: an Overview, *Int. J. Hydrogen Energy*, 2020, **45**, 3847.

16 Z. Cheng, J. Gao, Q. Fu, C. Li, X. Wang, Y. Xiao, Y. Zhao, Z. Zhang and L. Qu, Interconnected Molybdenum Carbide-Based Nanoribbons for Highly Efficient and Ultrastable Hydrogen Evolution, *ACS Appl. Mater. Interfaces*, 2017, **9**, 24608.

17 J. A. Schaidle, A. C. Lausche and L. T. Thompson, Effects of Sulfur on Mo_2C and Pt/Mo_2C Catalysts: Water Gas Shift Reaction, *J. Catal.*, 2010, **272**, 235.

18 R. A. Mir, S. Upadhyay and O. P. Pandey, A Review on Recent Advances and Progress in $Mo_2C@C$: a Suitable and Stable Electrocatalyst for HER, *Int. J. Hydrogen Energy*, 2023, **48**, 13044.

11342 | *J. Mater. Chem. A*, 2026, **14**, 11332–11343

This journal is © The Royal Society of Chemistry 2026

19 Z. Zhuang, J. Huang, Y. Li, L. Zhou and L. Mai, The Holy Grail in Platinum-Free Electrocatalytic Hydrogen Evolution: Molybdenum-based Catalysts and Recent Advances, *ChemElectroChem*, 2019, **6**, 3570.

20 Y. Li, Z. Yin, X. Liu, M. Cui, S. Chen and T. Ma, Current Progress of Molybdenum Carbide-based Materials for Electrocatalysis: Potential Electrocatalyst with Diverse Applications, *Mater. Today Chem.*, 2021, **19**, 100411.

21 L. Ma, L. Rui Lin Ting, V. Molinari, C. Giordano and B. Siang Yeo, Efficient Hydrogen Evolution Reaction Catalyzed by Molybdenum Carbide and Molybdenum Nitride Nanocatalysts Synthesized via the Urea Glass Route, *J. Mater. Chem. A*, 2015, **3**, 8361.

22 S. Jing, L. Zhang, L. Luo, J. Lu, S. Yin, P. Kang Shen and P. Tsiakaras, N-doped Porous Molybdenum Carbide Nanobelts as Efficient Catalysts for Hydrogen Evolution Reaction, *Appl. Catal., B*, 2018, **224**, 533.

23 Y. Huang, Q. Gong, X. Song, K. Feng, K. Nie, F. Zhao, Y. Wang, M. Zeng, J. Zhong and Y. Li, Mo_2C Nanoparticles Dispersed on Hierarchical Carbon Microflowers for Efficient Electrocatalytic Hydrogen Evolution, *ACS Nano*, 2016, **12**, 11337.

24 M. Kuang, W. Huang, C. Hegde, W. Fang, X. Tan, C. Liu, J. Ma and Q. Yan, Interface Engineering in Transition Metal Carbides for Electrocatalytic Hydrogen Generation and Nitrogen Fixation, *Mater. Horiz.*, 2020, **7**, 32.

25 G. Vitale, M. L. Frauwallner, C. E. Scott and P. Pereira-Almao, Preparation and Characterization of Low-Temperature Nano-Crystalline Cubic Molybdenum Carbides and Insights on their Structures, *Appl. Catal., A*, 2011, **408**, 178.

26 K. Guy, Synthèse de Nitrures et Carbures de Molybdène à partir de Clusters Métalliques : Applications en Catalyse Hétérogène, PhD thesis, Université de Rennes 1, 2020.

27 K. Guy, F. Tessier, H. Kaper, F. Grasset, N. Dumait, V. Demange, M. Nishio, Y. Matsushita, Y. Matsui, T. Takei, D. Lechevalier, C. Tardivat, T. Uchikoshi, N. Ohashi and S. Cordier, Original Synthesis of Molybdenum Nitrides Using Metal Cluster Compounds as Precursors: Applications in Heterogeneous Catalysis, *Chem. Mater.*, 2020, **32**, 6026.

28 W. Preetz, K. Harder, H. G. von Schnering, G. Kliche and K. Peters, Synthesis, Structure and Properties of the Cluster Anions $[(Mo_6Cl_8^i)X_6^a]^{2-}$ with X^a=F, Cl, Br, I, *J. Alloys Compd.*, 1992, **183**, 413.

29 A. Flemström, T. K. Hirsch, L. Sehlstedt, S. Lidin and L. Ojamäe, Effects from Hydrogen Bonds on Water structure in $(H_3O)_2[Mo_6Cl_8X_6] \cdot yH_2O$ X=Cl (y=7), Br (y=6), or I (y=6), *Solid State Sci.*, 2002, **4**, 1017.

30 H. T. Evans, B. M. Gatehouse and P. Leverett, Crystal Structure of the Heptamolybdate(VI) (paramolybdate) ion, $[Mo_7O_{24}]^{6-}$, in the Ammonium and Potassium Tetrahydrate Salts, *J. Chem. Soc., Dalton Trans.*, 1975, **6**, 505.

31 J. C. Sheldon, Chloromolybdenum(II) Compounds, *J. Chem. Soc.*, 1960, 1007.

32 F. W. Koknat, T. J. Adaway, S. I. Erzerum and S. Syed, Convenient Synthesis of the Hexanuclear Molybdenum(II) Halides Mo_6Cl_{12} and $Mo_6Br_{12} \cdot 2H_2O$, *Inorg. Nucl. Chem. Lett.*, 1980, **16**, 307.

33 A. W. Maverick, J. S. Najdzionek, D. MacKenzie, D. G. Nocera and H. B. Gray, Spectroscopic, Electrochemical, and Photochemical Properties of Molybdenum(II) and Tungsten(II) Halide Clusters, *J. Am. Chem. Soc.*, 1983, **105**, 1878.

34 A. N. Christensen, A Neutron Diffraction Investigation on a Crystal of α-Mo_2C, *Acta Chem. Scand.*, 1977, **31**, 509.

35 S. Chaitoglou, R. Ospina and E. Bertran-Serra, Cluster Mo_2C Deposited on Graphene Nanowalls by X-ray Photoelectron Spectroscopy, *Surf. Sci. Spectra*, 2024, **31**, 014001.

36 H. Vrubel and X. Hu, Molybdenum Boride and Carbide Catalyze Hydrogen Evolution in both Acidic and Basic Solutions, *Angew. Chem., Int. Ed.*, 2012, **51**, 12703.

37 Q. Cao, L. Zhao, A. Wang, L. Yang, L. lai, Z. Wang, J. Kim, W. Zhou, Y. Yamauchi and J. Lin, Tailored Synthesis of Zn–N co-Doped Porous MoC Nanosheets towards Efficient Hydrogen Evolution, *Nanoscale*, 2019, **11**, 1700.

38 H. Lin, Z. Shi, S. He, X. Yu, S. Wang, Q. Gao and Y. Tang, Heteronanowires of MoC–Mo_2C as Efficient Electrocatalysts for Hydrogen Evolution Reaction, *Chem. Sci.*, 2016, **7**, 3399.

39 T. Wei, T. Zhang, Z. Jin, F. Li and L. Xu, Fabrication of Nanocomposite MoC–$Mo_2C@C/Cd_{0.5}Zn_{0.5}S$: Promoted Electron Migration and Improved Photocatalytic Hydrogen Evolution, *Dalton Trans.*, 2022, **251**, 11397.

40 R. Michalsky, Y. Zhang and A. P. Peterson, Trends in the Hydrogen Evolution Activity of Metal Carbide Catalysts, *ACS Catal.*, 2014, **4**, 1274.

41 X. Zhang, J. Wang, T. Guo, T. Liu, Z. Wu, L. Cavallo, Z. Cao and D. Wang, Structure and Phase Regulation in Mo x C (α-MoC 1-x/β-Mo2 C) to Enhance Hydrogen Evolution, *Appl. Catal., B*, 2019, **247**, 78.

42 W. N. Wilson, J. M. Lane, C. Saha, S. Severin, V. S. Bharadwaj and N. Rai, Nature of Molybdenum Carbide Surfaces for Catalytic Hydrogen Dissociation using Machine-Learned Potentials: an Ensemble-Averaged Perspective, *Catal. Sci. Technol.*, 2025, **15**, 1492.

43 P. Schlexer Lamoureux, A. R. Singh and K. Chan, pH Effects on Hydrogen Evolution and Oxidation over Pt(111): Insights from First-Principles, *ACS Catal.*, 2019, **9**, 6194.

44 H. Prats and K. Chan, The Determination of the HOR/HER Reaction Mechanism from Experimental Kinetic Data, *Phys. Chem. Chem. Phys.*, 2021, **23**, 27150.

45 F. Tessier, Determining the Nitrogen Content in (Oxy)Nitride Materials, *Materials*, 2018, **11**, 1331.

This journal is © The Royal Society of Chemistry 2026

J. Mater. Chem. A, 2026, **14**, 11332–11343 | **11343**